P44 **TRACKING SUPERCELLS in TROPICAL CYCLONES**

Roger Edwards[1], Matthew D. Flournoy[2], and Mateusz Taszarek[3]

[1]Storm Prediction Center, Norman, OK
[2]National Severe Storms Laboratory, Norman, OK
[3]Adam Mickiewicz University, Poznań, Poland

1. INTRODUCTION and BACKGROUND

a. Tornadoes and supercells in tropical cyclones

In the conterminous U.S. (CONUS), tropical cyclones (TCs) often—but not always—produce tornadoes as they approach the coast closely enough for outer-band supercells to move ashore. Tornado production—typically in daytime-peaking cycles—may persist throughout the landfall phase, and for as many days inland as an identifiable warm-core circulation lingers after their landfall phases (Edwards 2012, hereafter E12). Tornadoes can cause casualties and produce damage well removed from the TC core region, sometimes in areas far from substantial gradient-wind and surge effects, and also well inland during TC decay stages, when the TC surface winds are decreasing, but low-level shear remains strong (E12). They account for a small, yet important, fraction of TC fatalities (about 3%; Rappaport 2014), and a substantial fraction of U.S. tornadoes in late summer to early autumn (Edwards et al. 2012a). As such, TC tornadoes long have been an important component of Storm Prediction Center (SPC) forecasting efforts (Weiss 1987; Edwards 1998).

TC tornado frequency can change strongly, whether within individual TCs from day to day (e.g., Nowotarski et al. 2021), from TC to TC in a season, or from year to year, and is only loosely related to the number of landfalling events (E12; Edwards and Mosier 2022, hereafter EM22). Strong variability in tornado production among TCs is related in part to synoptic-scale to mesoscale environmental factors that can vary from one system to another, including TC size (Paredes et al. 2021) and intensity (McCaul 1991), inland environmental changes (Schenkel et al. 2021), frontal interactions (Edwards and Pietrycha 2006), and effects of ambient deep shear (as measured through the 850–200-hPa pressure layer). The latter influences both 1) the distribution of convection and 2) the size and strength of supercell-favoring environments within the TC (Schenkel et al. 2020). These factors appear to account for the strong climatological signal of tornadoes in the middle to outer northeastern quadrant of CONUS TCs, and more generally, north through southeast of center (e.g., Verbout et al. 2007; E12).

Compared to their midlatitude counterparts, TC supercells and their mesocyclones tend to be smaller in horizontal and vertical extent, and as such, more difficult to detect at longer radar range due to beam-filling and -height considerations (e.g., Spratt et al. 1997; Eastin and Link 2009; Edwards and Picca 2016). Radar-detected, azimuthal shear in TC supercells often strengthens as they move onshore (Alford et al. 2023). This relates to near-coastal frictional effects on wind that enhance lower-tropospheric shear amid favorable ambient deep shear (Schenkel at al. 2021), as well as increased storm-scale convergence in that environment (Alford et al. 2023). The onshore mesocyclone intensification likely contributes to a long-observed near-coastal climatological maximum in tornado reports compared to inland (e.g., Hill et al. 1966; Schultz and Cecil 2009; E12; EM22), recognizing that tornadoes (waterspouts) offshore go almost entirely unrecorded (E12). When close enough to a WSR-88D unit–a varying but typically lesser distance than with most non-TC supercells—tornadic debris signatures (TDSs) can be detected via the dual-polarization, cross-correlation coefficient product (Rhyzhkov et al. 2005; Edwards and Picca 2016).

All the factors above render TC tornadoes both an important and often difficult problem in near-term forecasting and warning operations. So does the lack of published understanding of supercell motion in TCs, tornadic or not.

b. Supercell tracking and movement

Manual tracking of TC supercells and their radar-derived azimuthal shear has been conducted in an operational setting since the advent of the WSR-88D (e.g., Spratt et al. 2008). In research, tornadic TC supercells have been followed to evaluate TC-relative positioning and mesoscale environmental parameters (Edwards et al. 2012a), and to assess cell characteristics near the time of tornadoes and coastal interactions (Alford et al. 2023). However, tracking has not been done systematically with nontornadic TC supercells, or with nontornadic supercells in general (Flournoy et al. 2024, this conference, hereafter F24). The F24 project plans to alleviate this community need by manually tracking all CONUS supercell mesocyclones from 2022–2023.

[1] *Corresponding author address:* Roger Edwards, Storm Prediction Center, National Weather Center, 120 DL Boren Blvd #2300, Norman, OK 73072; E-mail: roger.edwards@noaa.gov, tornado.specialist@gmail.com (2025 onward)

Given operational experience of the lead author and results cited above, we hypothesize that a substantial majority of TC supercells (≥75%) are non-tornadic, as has been documented with midlatitude, non-TC supercells (Trapp et al. 2005). We also hypothesize that TC supercells follow tracks somewhat between those predicted by established operational algorithms for net cell motion in midlatitude, baroclinically regulated, non-TC situations, and ambient mean "steering" flow, the latter being more tightly cyclonic and intense with decreasing distance from TC center. In other words, TC supercell motion should be less deviant than (algorithms used to predict) that of their midlatitude counterparts, based on both operational experience and the results of low-CAPE, low-LFC, small LCL–LFC subsets of simulations in Kirkpatrick et al. (2007) that they used to approximate a typical TC supercell environment (McCaul 1991). [McCaul and Weisman (2001) simulated TC supercells explicitly, but did not test environmental effects on their movement.]

As for storm-motion algorithms, the "internal dynamics" method developed by Bunkers et al. (2000; hereafter B00) is the most common in U.S. operational sounding-analysis software, such as SHARPpy (Blumberg et al. 2017), its predecessor at SPC, NSHARP (rooted in a PC-based package called SHARP; Hart et al. 1991), and BUFKIT (Mahoney and Niziol 1997). The same algorithm is used in other tools such as the R-language-based freeware package "thundeR" (Taszarek et al. 2023), which is optimized for assessment of the European Centre for Medium-Range Weather Forecasts reanalysis, version 5 (ERA5, Hersbach et al. 2020), and also employed herein (below).

Before B00, a common motion predictor was the Maddox (1976; hereafter M76) "30R75" scheme, which stood for 30° rightward of the mean-wind direction, and 75% of the speed. This was based on 179 observed, non-TC soundings launched at ≈2315 UTC, within a 92.5-km radius of a tornado recorded between 2200–0100 UTC. Unlike most techniques since, M76 computed "mean wind" by averaging observed wind components at mandatory reporting levels (surface, 850, 700, 500, 300, and 200 hPa). For consistency in comparison with the other motion methods, we use the 0–6-km mean wind (MW) more common to supercell-motion techniques deployed since, when computing and evaluating 30R75.

Another storm-motion technique that was developed by Davies and Johns (1993, hereafter DJ93) used a "20R80" method—20° rightward and 75% of MW—for 0–6-km MWs >15 m s^{-1}. In DJ93 and follow-up studies (e.g., Davies 1998), weaker MWs were assigned more strongly deviant motions (smaller speeds, larger rightward directional shift). However, given that most TC tornadoes occur amid gale-force (34–47 kt or 17.5–24.2 m s^{-1}) and stronger *surface* winds of TCs—which are weaker than winds aloft (including MW) due to frictional effects over land where tornadoes are reported (E12)—the weaker-wind motion estimates are not used herein.

Section 2 discusses the TC supercell and tornado data analyzed herein, the case example to which it is applied, and the methods for that analysis. Section 3 describes the results, and section 4 offers conclusions and discussion for additional work.

2. CASE DATA and METHODS

The F24 track dataset is intended to include supercells in any meteorological regimes, including TCs. Given the large number of supercells and/or tornadoes that some TCs can produce (e.g., Spratt et al. 1997; Eastin and Link 2009; Edwards 2012; Edwards et al. 2012a), we sought a recent case of an "efficient producer" with numerous apparent supercells, conforming to the broader study timeframe of F24 in general. Hurricane Ian of 2022—in Florida and North Carolina—fit the desired apparent activity level, and serves as a proof of concept for the application of F24 techniques to TC settings.

a. Hurricane Ian and its tornadoes

Bucci et al. (2023) detail Ian's track, intensity and multi-hazard impacts. In summary, Ian formed in a strong tropical wave that exited west Africa on 14–15 September 2022, becoming a tropical storm in the central Caribbean Sea at 0000 UTC 24 September, and a hurricane after turning northwestward across the northwestern Caribbean, by 0600 UTC 26 September. Ian crossed western Cuba within a few hours after becoming a major (Category 3; Schott et al. 2022) hurricane, at 0600 UTC 27 September. From Cuba across the eastern Gulf of Mexico, Ian took a north-northeastward path toward southwestern Florida. Ian's horizontal size expanded in response to an eyewall-replacement cycle that also, unusually, led to central intensification. Ian peaked as a 140-kt (72m s^{-1}) Category 5 hurricane at 1200 UTC 28

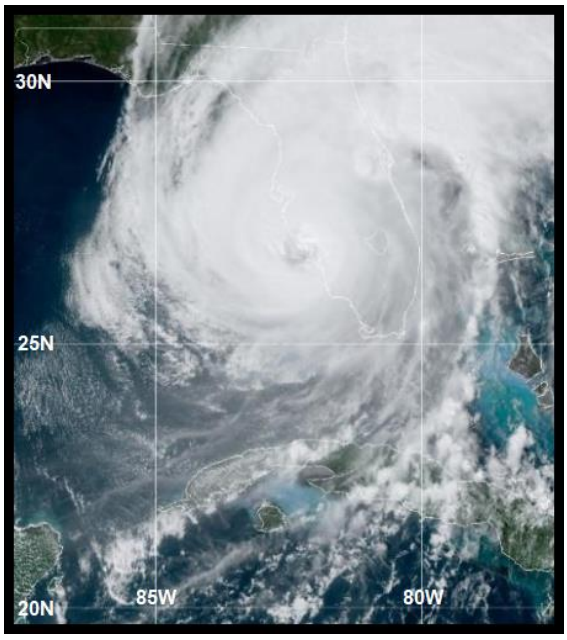

Figure 1: GOES-16 "geocolor" visible image of Hurricane Ian near landfall, 1910 UTC 28 September 2022. Adapted from Bucci et al. (2023).

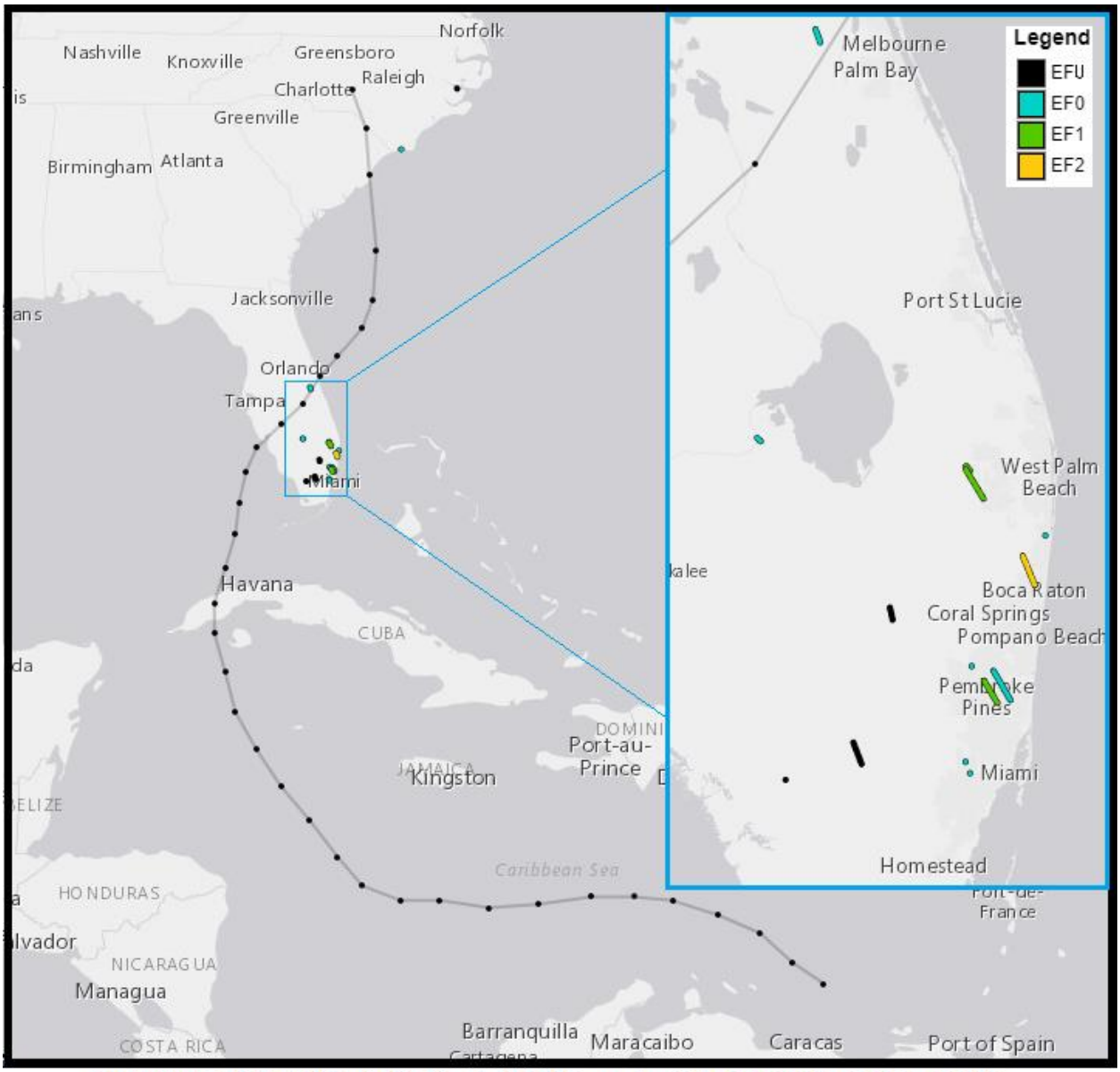

HURRICANE IAN (2022) TRACK and TORNADO LOCATIONS

Figure 2: Center track of Hurricane Ian (gray), with dots representing tornadoes and colored according to their damage rating (legend in inset). EFU corresponds to EF-unknown (Edwards et al. 2013). The inset expands the tornadic domain over east-central and southern Florida for better path resolution. Maps adapted from the SPC TC tornado online plotter (Mosier and Edwards 2022).

September. It then weakened, made initial Florida landfall at Cayo Costa (Fig. 1) around 1905 UTC, then moved inland near Punta Gorda, FL, around 2035 UTC, with peak eyewall wind of 125 kt (64 m s^{-1}).

Ian weakened to a 60-kt (31 m s^{-1}) tropical storm while passing northeastward across peninsular Florida. As a highly asymmetric TC, with most deep convection over its northern semicircle, Ian strengthened again over the Atlantic Ocean. Ian reached a second peak central intensity of 70 kt (36 m s^{-1}), a Category 1 hurricane, by the time of its second mainland landfall near Georgetown, SC, at 1805 UTC 30 September. Ian then merged with a frontal zone in North Carolina, becoming a decaying extratropical cyclone by 0000 UTC 1 October.

Tornado reports for Ian come from the national TC tornado dataset (TCTOR), described and illustrated in EM22. In short, TCTOR is derived from the national SPC tornado database, which in turn consists of county-based path segments gathered by NCEI from local NWS offices. At SPC, those segments are stitched together where crossing county lines to yield one path per tornado, then combined to one path entry in TCTOR where crossing state lines, unlike in the SPC dataset (Edwards et al. 2022). TCTOR then includes hurricane-track data prepared by NHC after each season, interpolated to tornado time, with center-relative tornado geometry also computed. Those data permit TC-motion-relative computation of tornado positions with respect to center, as well as true-north-relative plotting.

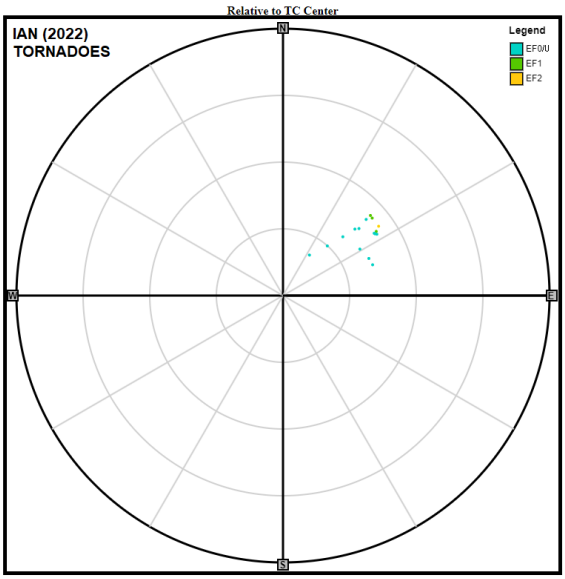

Figure 3: Polar plot of tornado starting positions in Hurricane Ian relative to TC center (origin) and true north (up, labeled N). Range rings (gray) are every 100 km, with azimuthal lines every 30°. Tornado positions are colored by damage rating (legend).

Ian produced two rounds of landfall-stage tornadoes: 14 on 27–28 September over southern and central Florida, and two more on 30 September over eastern North Carolina (Fig. 2). They conformed to aforementioned downshear, northeastern climatological locations with respect to center (E12; Schenkel et al. 2020), but concentrated more to middle-inner radii (inside 400 km, Fig. 3). As such, Ian's Florida tornadoes were pre-landfall, except for one in east-central Florida west of Melbourne, about 25 min after landfall. The North Carolina tornadoes occurred ≈1.5 h before and ≈1.25 h after South Carolina landfall. The locations and times of all these tornadoes, along with preliminary, automated estimates of supercell tracks (section 2b), set loose spatiotemporal windows for where and when radar-observed supercells would be most probable.

Since nonsupercell radar echoes account for just ≈12% of tornado reports in TCs, and are distributed similarly to supercells in TCs (Edwards et al. 2012b), we use tornadoes as a general clue to investigate for supercells overall, in addition to the automated guidance. Manual tracking revealed that one of Ian's tornadoes was not associated with a supercellular radar echo: west of Lake Okeechobee at 0625 UTC 28 September (westernmost EF0 tornado in the Fig. 2 inset). All other tornadoes were supercellular.

The NSSL multi-radar/multi-sensor (MRMS) suite (Smith et al. 2016) includes a three-dimensional mosaic with 33 vertical levels, consisting of radar-derived and severe-weather-related variables at 0.01° latitude × 0.01° longitude, compiled ever 2 min across the CONUS. MRMS includes azimuthal-shear data that can be thresholded and used to perform approximate supercell tracking, including sampling in the 0–2-km (lower tropospheric) and 3–6-km (midtropospheric) AGL layers for its "rotation tracks" product. Despite the relative shallowness of TC supercells, they often extend enough into the 3–6-km layer to be "first-guess" tracked this way. However, for those that do not, tracking of TC supercells with only "low-level" (>3-km deep) mesocyclones via manual means still ensures fuller sampling and time continuity of their paths than MRMS-based automated techniques. For each case day in F24, MRMS-based tracks of azimuthal shear are used as a first-guess field. That was true to limited extent for the Hurricane Ian event, though the density, overlapping and overall messiness (ultimately, overproduction) of "AzShear" first-guess tracks (Fig. 4) ensured only a broader, mesoscale region to be checked for supercells, instead of attempts to compare individual tracks.

b. Supercell tracking methods

F24 describe in detail the data-gathering and analysis techniques and CONUS-wide background for their broader project to track supercells. In general, the same tracking philosophy and techniques are employed here, but with some modifications to the F24 rules to account for the relative spatiotemporal smallness of many TC supercells. For example, the "midlevel mesocyclone" of a TC supercell, or even its echo top, may be well below the middle troposphere in the TC environment, with a middle-*supercell* layer as low as ~1–2 km AGL. Others barely extend into the MRMS-standard 3–6-km "midlatitude" midlevel layer defined in Smith et al. (2016). In addition to limiting the fidelity of MRMS-based azimuthal-shear tracking, which is used as first-guess input for F24 (and to some extent, here), the shallowness of ≥30-db*Z* echoes and mesocyclones near landfall often compels using observed single-radar data from <3 km above radar level (ARL) for establishing horizontal, scan-to-scan mesocyclone continuity. At the volume scan of apparent genesis, each mesocyclone was tagged with a sequential number (1, 2, 3, etc.). The demise circumstance of each supercell was recorded: dissipation, upscale evolution, merger with another supercell, or merger with a nonsupercellular convective cluster.

Tracking of observed supercells began with examination of single-site WSR-88D data taken from the NCEI-supplied, Amazon Web Services™ archive "bucket" of raw WSR-88D Level-2 data (https://noaa-nexrad-level2.s3.amazonaws.com/index.html), viewed with GRLevel2™ software produced by Gibson Ridge Software, LLC. The software allows a full-tilt, multi-panel, position-matching examination of all available base moments and derived fields, including those specific to dual polarization, across all beam tilts, and from volume scan to volume scan. This versatility enabled both forward- and backward-tracking of a supercell to its demise and origin, once an embedded mesocyclone was found.

Cells were followed and paths mapped from the location of the first ≥30-db*Z* echo, through production of one or more mesocyclones, to the demise of the supercell. Brief, weak, transient, along-beam shear features were common in TC echoes, even those of amorphous, non-cellular character, and were not counted as mesocyclones. Mesocyclones had to have trackable spatiotemporal continuity across

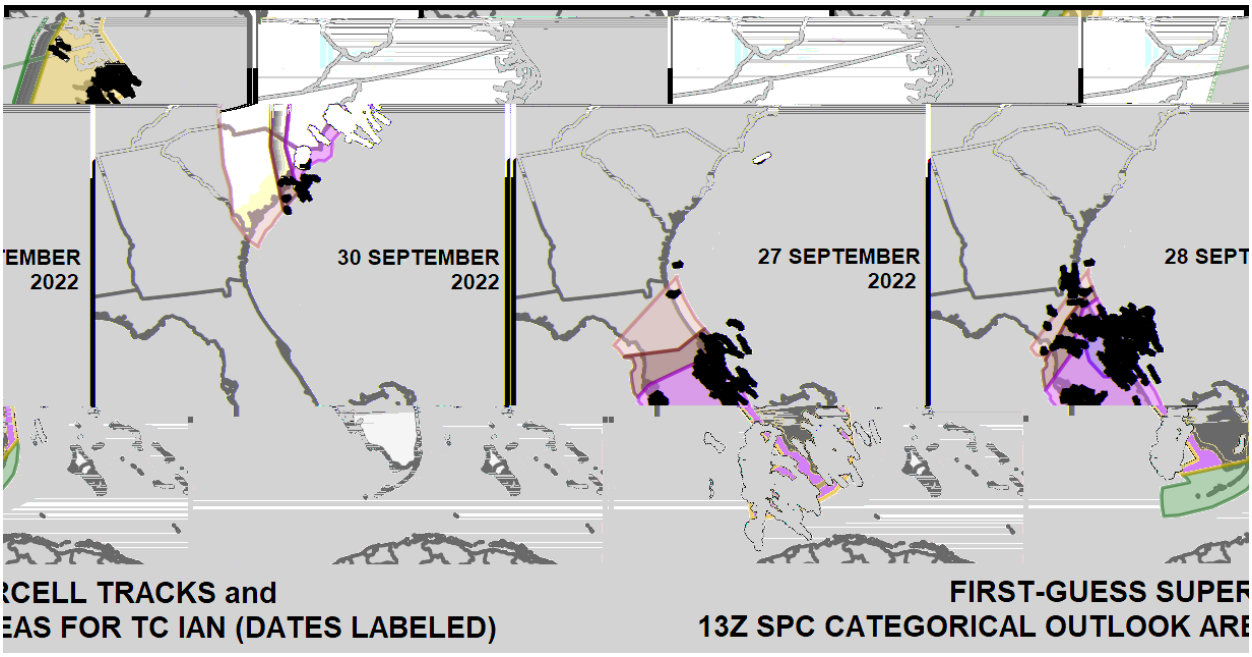

Figure 5: First-guess, MRMS-derived "AzShear" tracks (black) for the Florida (left and middle) and Carolinas (right) phases of TC Ian, overlaid with SPC day-1 categorical outlook areas (described in Edwards et al. 2015) issued at 1300 UTC on the labeled days. Orange represents "Enhanced Risk" (10% probabilistic) tornado potential, yellow is "Slight Risk" (5%), dark green is "Marginal Risk" (2%), and light green is the general-thunderstorm forecast.

multiple scans. This resulted in 54 tracked supercells, 39 being in Florida, with the balance occurring in North Carolina. Mesocyclone tracks associated with these supercells, along with tornado locations, are mapped in Fig. 6. Apparent track gaps are between mesocyclones, and the mapped tracks do not show pre-mesocyclone, organizational stages of cells. Zigzags and similar irregularities in mesocyclone tracks—especially near their end—may be related to:

- Raising or lowering of the beam elevation needed to ascertain a vertically tilted mesocyclone optimally—usually while forming, decaying or when the supercell translated with a substantial along-beam component (toward or away from the radar);
- Positional uncertainty in weak and/or broadening mesocyclones;
- Uncertainty or error in centering close-proximity, simultaneous mesocyclones or cyclic "handoff" processes, especially when they were far from a radar or otherwise exhibiting ambiguous form.

To define a representative motion vector for each supercell's mature stage, metric(s) of peak intensity of organization were needed for a radar volume scan (reference scan) around which to center the motion computation. Full volume scans can vary slightly in duration, depending on scan strategy, so we chose a number of full scans (±3 either side of the reference scan) instead of a rigid timeline. This allowed for at least half an hour, and typically near 40 min of reference tracking to compute a cell-motion vector. While acknowledging the nonlinearity and innate subjectivity in supercell-motion analysis, this strategy allowed for a "Goldilocks zone" of consistently defining motion that was neither short enough to be strongly influenced by a transient, 1–2-scan wobble, nor long enough to exceed a supercell's lifespan.

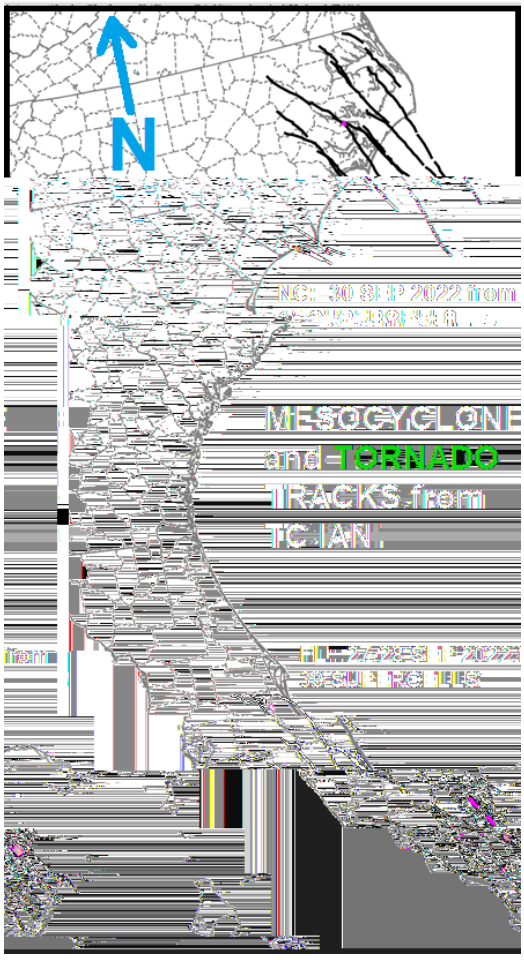

Figure 6: Mesocyclone tracks (black) and tornado reports (magenta) from 54 supercells of TC Ian, in Florida (bottom) and North Carolina (top).

Figure 7: Flow chart (left to right) for choosing a reference scan to anchor the supercell-motion computation.

Table 1: Median values for 15 tornadic (red) and 39 nontornadic (blue) supercells, of (left to right) number of volume scans during supercell lifespans, observed motion direction (OBS DIR), observed speed (OBS SPD), then absolute speed and direction errors (ERR) for 0–6-km AGL mean wind, B00 motion, 30R75, and 20R80.

SUPERCELL CLASS	SCANS	OBS DIR (°)	OBS SPD (m/s)	MW DIR ERR (°)	MW SPD ERR (m/s)	B00 DIR ERR (°)	B00 SPD ERR (m/s)	30R75 DIR ERR (°)	30R75 SPD ERR (m/s)	20R80 DIR ERR (°)	30R75 SPD ERR (m/s)
TORNADIC	26.5	332	12.7	1.3	6.4	17.1	2.6	31.3	2.0	21.3	2.9
NONTORNADIC	17	330	14.7	0.0	5.8	18.7	0.4	30.0	0.9	20.0	1.7

Defining the reference scan was performed as depicted in Fig. 7. Priority went to tornadoes, and if more than one per supercell, the highest-rated. One supercell in North Carolina had no reported tornadoes, but did produce a nearshore waterspout, spotted during the 1800 UTC 30 September Morehead City (KMHX) reference scan. Barring observed tornadic vortices, a nontornadic TDS is prioritized next. One supercell in Florida exhibited an apparent TDS without corresponding tornado report, during the 1848 UTC 28 September Melbourne (KMLB) reference scan (not shown). Otherwise, the peak along-beam rotational-velocity magnitude (V_{rot}) for the ongoing targeted scan height range was analyzed as in Smith et al. (2015). Note that this may not be the peak V_{rot} for the entire supercell at all possible beam elevations and times. Instead, this is the max V_{rot} found during the usual attempt to remain on a beam height representing "midlevel" with respect to supercell depth, in keeping with the F24 ideal.

Once the positions from ±3 scans either side of the reference scan were used to compute each supercell's observed motion vector, they could be compared to those from the motion algorithms. In general, ERA5 reanalysis well represents TC track, size, structure, and environment in and near the CONUS (Schenkel and Hart 2012; Murakami 2014; Hodges et al. 2017; Schenkel et al. 2017). We therefore use ERA5 grids to generate tornado-proximity "point" soundings, and for comparing motion techniques to observed motion. The MW and B00 motions were calculated using thundeR from reanalysis soundings in the ERA5 grid box containing the reference scan for each supercell. Then 30R75 and 20R80 vectors were computed off the ERA5 MW valid at each reference scan. With these steps done, comparisons could be made among the storm-motion algorithms (section 3a), and examinations could be performed of supercell environments (section 3b).

3. PRELIMINARY RESULTS

a. Supercell-motion and timeline characteristics

Ian's tornadoes—both in Florida and North Carolina—occurred in a tightly constrained sector of the cyclone northeast of center (Fig.3). This was in a land-limited part of both southern and eastern Florida and eastern North Carolina located to the downshear right of the path (Schenkel et al. 2020), south of areas of more-stable, rain-cooled boundary-layer air, and within very moist, relatively convectively unmodified maritime-tropical fetches from the Caribbean Sea and Atlantic Ocean, respectively (more in section 3b).

Despite the airmass and land-area constraints, Ian produced 54 trackable supercells (Fig. 6). Of those, 16 (30%) were flagged as tornadic for analysis purposes, including the supercells with a no-report TDS (Florida) and spotted waterspout (North Carolina). Fourteen (26%) were tornadic by actual reports. These percentages are roughly consistent with our midlatitude-supercell-based hypothesis, albeit on a very limited case sampling of one TC. The longest supercell lasted 56 scans and ≈6 h (1449–2055 UTC 30 September, tornadic, KMHX radar, NC), then dissipated. The shortest only was identifiable for 9 scans (1555–1640 UTC 30 September, tornadic, KLTX radar at Wilmington, NC). It passed directly over the radar for one unsampled scan, then dissipated. Four supercells needed two radars each to track: three passing from the domain of Miami (KAMX) to Melbourne (KMLB), FL, and one from KMHX to Wakefield, VA (KAKQ).

The tornadic supercells' sample size is rather small for meaningful statistical distributions (Doswell 2007), necessitating more TCs. However, medians of each sample (Table 1) indicate tornadic supercells (including a waterspout and a TDS) lasted about 1.5 times longer and moved somewhat slower than nontornadic, with respect to MW, but both supercell classes moved essentially along the MW direction. As such, directional errors were similar for tornadic and nontornadic supercells within each algorithm. However, speed-estimate errors were at least slightly positive (too fast) for tornadic cells.

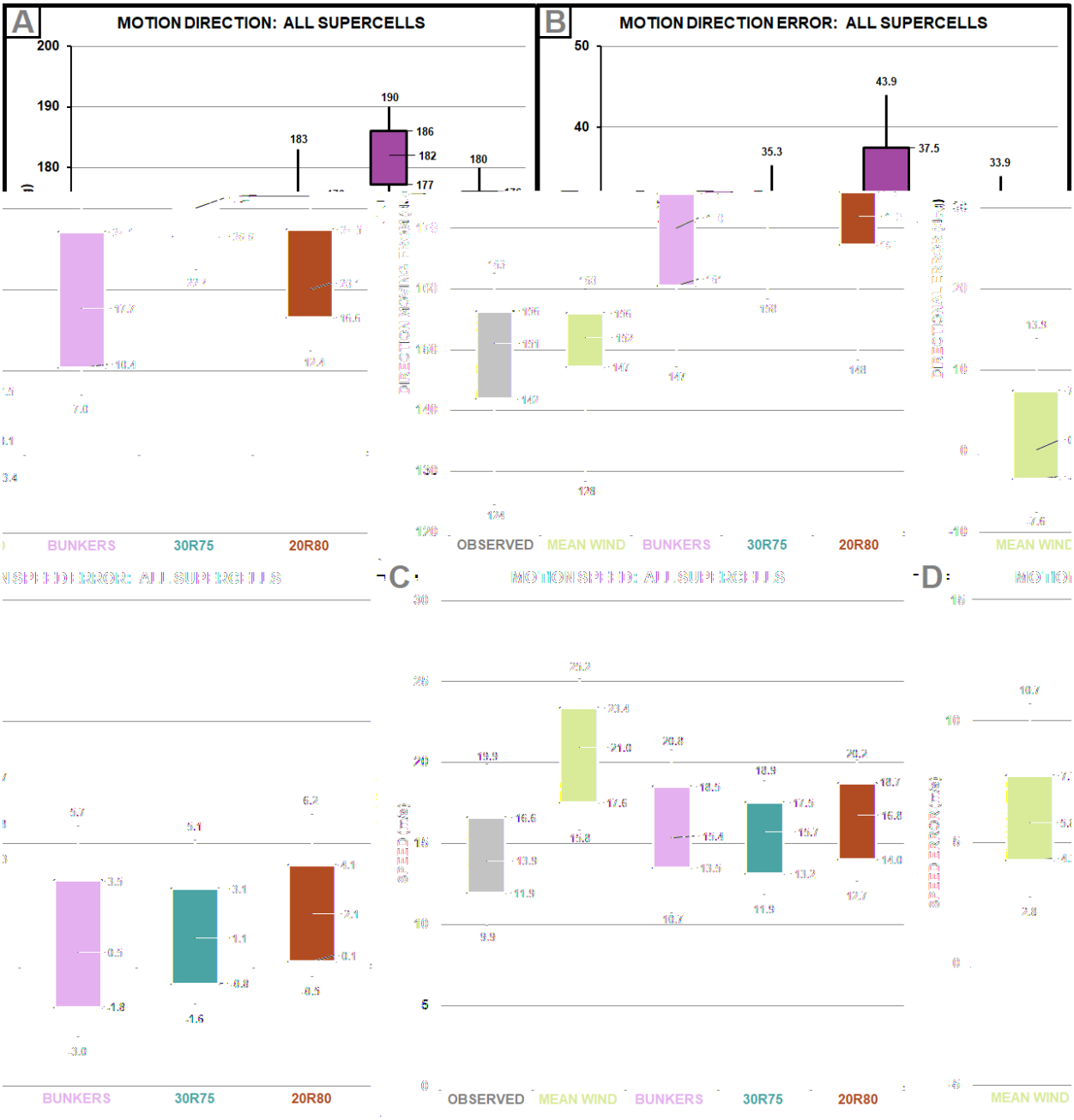

Figure 7: Box-and-whisker diagrams depicting the distributions of middle two quartiles (colored boxes, quartile values and medians provided) and 10th to 90th percentiles (whiskers, tip values provided) for: a) Azimuthal supercell motion (° from), b) azimuthal directional error (°) compared to observed, c) speed (vector magnitude, m s^{-1}), and d) speed error (m s^{-1}) compared to observed. Observed motions in (a) and (c) are gray, 0–6-km AGL mean wind in each panel is light blue, B00 motion ("Bunkers") is tan, 30R75 is purple, and 20R80 is green. Sample size is 54 supercells.

In bulk, Ian's supercells tended to move with MW directionally, but much slower, with the entire 10th-90th percentile MW distribution being too fast by 2–11 m s^{-1}. Observed supercells moved somewhat slower overall than any of the motion algorithms (Fig. 7), but with some lower-quartile extension into negative speed error (too slow) for 30R75 and 20R80 distributions. Put another way, the Bunkers, 30R75 and 20R80 algorithms all moved supercells slower, as expected, but too far to the right.

b. Supercell environments

Though environmental examination wasn't a specific objective of this study, it was undertaken as a beneficial offshoot of the effort to derive MW and B00 motions from ERA5 data, and will be summarized here. Supercell and tornado environments were sampled by sets of ERA5 soundings taken not only for the gridpoint hour of each supercell's reference

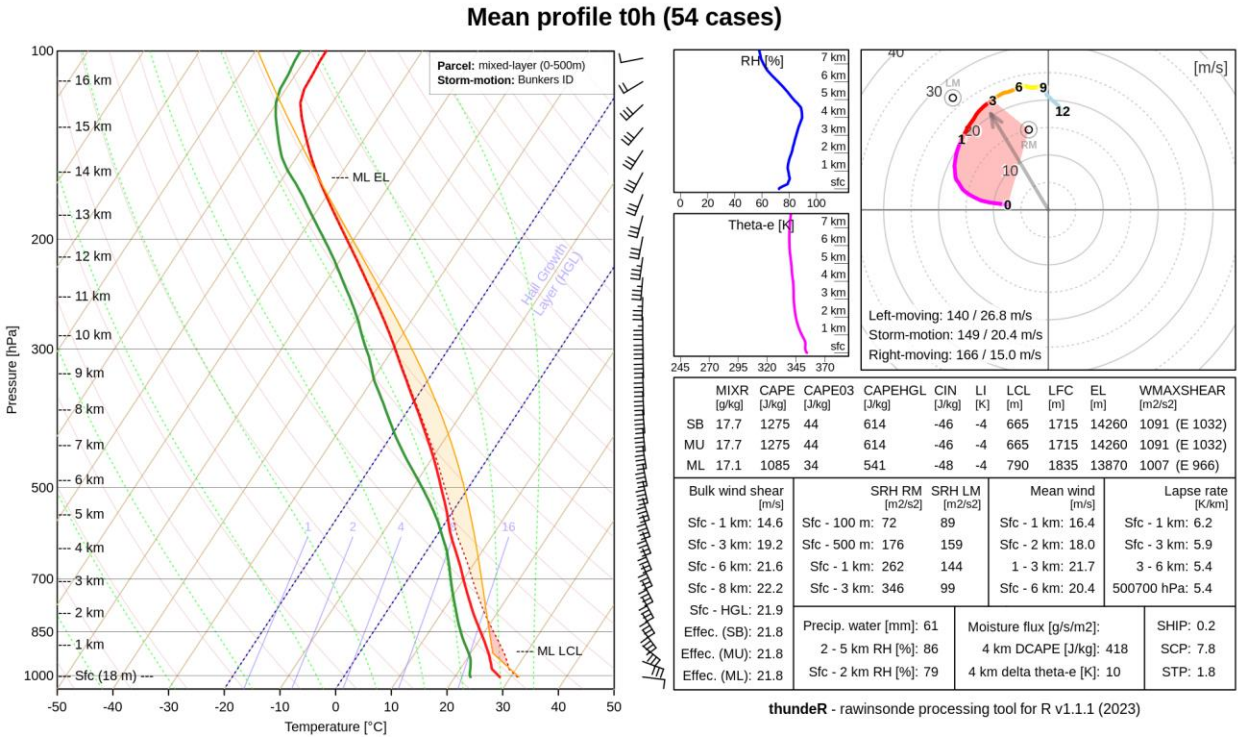

	MIXR [g/kg]	CAPE [J/kg]	CAPE03 [J/kg]	CAPEHGL [J/kg]	CIN [J/kg]	LI [K]	LCL [m]	LFC [m]	EL [m]	WMAXSHEAR [m2/s2]
SB	17.7	1275	44	614	-46	-4	665	1715	14260	1091 (E 1032)
MU	17.7	1275	44	614	-46	-4	665	1715	14260	1091 (E 1032)
ML	17.1	1085	34	541	-48	-4	790	1835	13870	1007 (E 966)

Bulk wind shear [m/s]	SRH RM [m2/s2]	SRH LM [m2/s2]	Mean wind [m/s]	Lapse rate [K/km]
Sfc - 1 km: 14.6	Sfc - 100 m: 72	89	Sfc - 1 km: 16.4	Sfc - 1 km: 6.2
Sfc - 3 km: 19.2	Sfc - 500 m: 176	159	Sfc - 2 km: 18.0	Sfc - 3 km: 5.9
Sfc - 6 km: 21.6	Sfc - 1 km: 262	144	1 - 3 km: 21.7	3 - 6 km: 5.4
Sfc - 8 km: 22.2	Sfc - 3 km: 346	99	Sfc - 6 km: 20.4	500700 hPa: 5.4
Sfc - HGL: 21.9				
Effec. (SB): 21.8	Precip. water [mm]: 61		Moisture flux [g/s/m2]:	SHIP: 0.2
Effec. (MU): 21.8	2 - 5 km RH [%]: 86		4 km DCAPE [J/kg]: 418	SCP: 7.8
Effec. (ML): 21.8	Sfc - 2 km RH [%]: 79		4 km delta theta-e [K]: 10	STP: 1.8

Figure 8: Mean ERA5 sounding generated by "thundeR" for all 54 supercellular reference scans for TC Ian, presented thermodynamically with vertical wind profile in a conventional skew T-log p diagram (left, winds in kt), hodograph with radii every 5 m s^{-1} (upper right), and table of calculated variables and parameters (lower right). On the sounding diagram, the orange are represents mixed-layer CAPE, with that value—along with those for surface-based and most-unstable parcels—given in the table at right. On the hodograph, values represent km AGL, gray vector represents MW, "RM" and "Right-moving" represent the B00 motion with accordingly assumed 0–3-km SRH area shaded, and B00-derived SRH values given in the table. Vertical profiles of relative humidity (RH, labeled) and θ_e (labeled) appear between the sounding diagram and hodograph. Click on image or this link for an animation (GIF format) of the mean soundings for supercell reference scans at time t ±6 h.

scan, but generated ±6 h from the hour of reference scan. This includes the genesis and demise of all the supercells, and at least 3 h before and after supercell lifespan. In general, given the fact that tornadoes occurred in each landfall phase, parameters in Ian unsurprisingly conformed well to climatological norms described in numerous prior studies (e.g., McCaul 1991; E12; Schenkel et al., 2020), with the most-favorable overlaps of buoyancy and low-level shear located in the eastern semicircle, and especially northeast of center. This was downshear with respect to the ambient deep (850–200 hPa) shear vector impinging on the TC as well (not shown). For the supercells in bulk, enlarged low-level (lowest 3-km, 1-km and 500-m) hodographs were apparent, with no concavities nor other evidence of substantial weaknesses in the wind and shear vectors comprising them (e.g., Fig. 8). Strong low-level bulk shear measures and other favorable values for kinematic parameters in Ian, typical for TC tornado settings, are displayed in the mean sounding of Fig. 8.

A 12-h animation of mean gridpoint soundings centered on reference scan is linked from Fig. 8. The loop shows that, from shortly before through after the passage of peaking supercells, hodographs tended to be largest between approximate storm genesis times and shortly after reference scans, veering around the origin through the 12-h sampling period, and shrinking after the reference scans. Various storm-relative helicity (SRH) measures (using B00 motion) peaked around the reference hours, as did a severe-weather parameter not designed for TC environments called WMAXSHEAR, that multiplies the square root of 2×CAPE (WMAX) and deep-layer shear (Taszarek et al. 2017). The mean-wind vectors veered from southeasterly to almost southerly with time, likely reflecting the veering of ambient TC flow that would be expected as the center passed southwest through west of the gridbox.

Thermodynamically, mid/upper-tropospheric lapse rates were near moist-adiabatic, as expected in a TC, offset by enough low-level θ_e to yield deep buoyancy, with typically low CAPE density (CAPE per layer of convective cloud depth; Edwards and Thompson 1998) for a TC. CAPE tended to be greatest near and after reference hour, overlapping with the largest values of most low-level shear and SRH measures around reference time. This, of course, is consistent with the notion of maximized supercell parameters in a grid box as a supercell passes through, and peak supercell organization during optimization of the mesoθ-scale CAPE-shear parameter space. Accordingly, the supercell composite and significant tornado parameters (SCP and STP respectively; Thompson et al. 2003) maximize around the reference hour.

Little variation was noted in supercell environments across the Florida or North Carolinas phases, except for warmer surface conditions and somewhat greater CAPE in the local late morning through afternoon (roughly 18-00 UTC) events. In Florida, this likely relates to subtle overland diabatic surface heating also noted at conventional observing sites (not shown), under Ian's cirrus deck and between convective bands evident in satellite imagery (e.g., Fig. 3). Accordingly, by reference scan, more supercells (59%) occurred during approximate local daylight (1200–2359 UTC) then overnight, despite the supercells' occurring in landfall phases when the sea is closest and access to maritime/tropical oceanic air is most direct. That said, all second-landfall (North Carolina) supercells were daytime, while all nocturnal supercells were in Florida. The share of daytime supercells in Ian was lower than the 68% overall rate of daytime TC tornadoes from 1995–2021 (Fig. 15 in EM22), which also includes all more-diurnal inland-decay tornadoes in that period.

4. CONCLUSIONS and DISCUSSION

Ian's observed supercell directions were on the MW, and as such, too far rightward in all the motion algorithms. Also with TC supercells being slower than MW and most like B00, the best predictor of TC supercell movement was a cross-utilization of MW direction and B00 speed. However, the 30R75 speed and speed-error distributions were similar enough to B00 and observed motions that the 75% part of 30R75 may be a reliable speed predictor as well.

Since this early work was limited to one TC—albeit one with many supercells—representativeness of our environmental and track-behavior findings across the broader spectrum of supercellular TCs is unclear. One potential precaution will need to be monitored explicitly, as both TC and national analyses continue. If other TCs' supercells systemically exhibit similar motion behavior to Ian's, especially in terms of not right-moving off the MW, TC events may need to be treated separately from in the larger database of F24 events, under the ideas that:

- A yet-undocumented physical process exists common to at least landfall-phase TCs that is preventing substantial right motion otherwise observed with midlatitude supercells; and
- TC supercells' directional MW conformity misleadingly could offset rightward deviances of non-TC supercells if the former are included in bulk, national-level analyses.

Further, since Ian was in landfall phases for both its supercell cycles, no conclusions can be drawn about inland-decay TC supercells yet. Inland-decay stages typically experience stronger deep shear and interactions with baroclinic processes (Schenkel et al. 2021; Trier et al. 2023) that can influence tornado potential and supercell behavior. Both phases will need comparison, in the event inland-decay stages exhibit right motion mode similar to non-TC supercells—which we hypothesize to be the case, given weaker ambient flow than landfalling systems. Only substantial further sampling of multiple TCs, landfalling and inland, can decide these issues.

To that end, more TCs from the dual-polarization WSR-88D era are planned for the extended research arising from F24. This should include other prolifically tornadic TCs near landfall(s) such as Milton of 2024 in Florida, and those with both near-coastal and inland tornadic supercell cycles (e.g., Beryl of 2024 and Harvey of 2017). Hypothetically—both from operational experience, and based on echo-top observations ancillary to TDS-depth evaluation (Edwards and Picca 2016)—inland TCs tend to produce deeper, larger supercells, with "midlevels" closer to their non-TC counterparts. Including more TCs and inland stages also will add diversity of cell widths, environments, morphologies, geography, and center-relative azimuthal/range diversity (the latter not present in Fig. 3 for Ian) to the dataset. Inclusion of multiple TCs from Texas (e.g., Harvey) to the Mid-Atlantic (e.g., Isaias of 2020) also will facilitate large-sample comparisons of supercell-motion characteristics, not only across the various TCs and landfall versus inland-decay stages, but between TC and non-TC supercells in the broader F24 project. Operationally, understanding gained from such research extensions of this preliminary work should aid in near-term forecasting ("nowcasting") of TC supercell behavior and appropriately precise spatiotemporal layout of tornado warnings, with minimized false-alarm area.

Mesoscale environmental characteristics have been shown to influence supercell motion (e.g., B00). ERA5 representations environmentally supported supercells and tornadoes in Ian's landfall phases, and obviously supported its supercells' tendency to align movement with the MW, but slower. How valid is this idea for larger or smaller TCs, and landfall or inland phases that produce many more or fewer tornadoes than Ian? Potential variability in supercell activity from TC to TC, or even from day to day in the same TC (e.g., Nowotarski et al. 2021), should be evaluated in context of ERA5 environmental differences, for "apples to apples" comparisons. Also, other means of evaluating TC tornado settings that are readily available in operations—such as the SPC "SFCOA" objective mesoanalysis (Bothwell et al. 2002)—can be used similarly to how ERA5 was here, including soundings from its base Rapid Refresh model (and predecessor Rapid Update Cycle). Comparisons of the same environments across SFCOA and ERA5, including with any observed soundings matching a grid box in each and proximal to supercells, can help to assess each platform's situational viability as a TC supercell environmental evaluation tool.

Finally, if our motion results are generalizable after analyzing more TCs, a high-resolution numerical-modeling study—as with the Cloud Model 1 (CM1; Bryan et al. 2003)—may help with understanding supercell motion in TCs. Variations of CM1 have been applied successfully to hurricanes for other purposes, such as simulating finescale influences on overall TC intensity and structure (e.g., Bryan and Rotunno 2009; Bryan 2012), and to midlatitude supercells' environmental sensitivities (e.g., Coffer and Parker 2017 among many others). This includes surface friction or drag (Markowski 2016), the onshore increase of which also has been linked to

enhancement of SRH and TC tornado production (Baker et al. 2009; Eastin and Link 2009). In turn, a CM1-based examination could be used to gauge physical influences on supercell movement and morphology in the TC.

REFERENCES

Alford, A. A., A. Messersmith, B. Pollock, Q. Thomas, T. N. Sandmael, and B A. Schenkel, 2023: Tropical cyclone supercell response to the coast using a climatology of radar-derived azimuthal shear. *Geophys. Res. Lett*., **50**, e2023GL105977, https://doi.org/10.1029/2023GL105977.

Baker, A. K., M. D. Parker, and M. D. Eastin, 2009: Environmental ingredients for supercells and tornadoes within Hurricane Ivan. *Wea. Forecasting*, **24**, 223–244, https://doi.org/10.1175/2008WAF2222146.1.

Blumberg, W. G., K. T. Halbert, T. A. Supinie, P. T. Marsh, R. L. Thompson, and J. A. Hart, 2017: SHARPpy: An open-source sounding analysis toolkit for the atmospheric sciences. *Bull. Amer. Meteor. Soc*., **98**, 1625–1636, https://doi.org/10.1175/BAMS-D-15-00309.1.

Bothwell, P. D., J. Hart, and R. L. Thompson, 2002: An integrated three-dimensional objective analysis scheme in use at the Storm Prediction Center. *21st Conf. on Severe Local Storms*, San Antonio, TX, Amer. Meteor. Soc., JP3.1, https://www.spc.noaa.gov/publications/bothwell/sfcoa.pdf.

Bryan, G. H., 2012: Effects of surface exchange coefficients and turbulence length scales on the intensity and structure of numerically simulated hurricanes. *Mon. Wea. Rev*., **140**, 1125–1143, https://doi.org/10.1175/MWR-D-11-00231.1.

——, and R. Rotunno, 2009: The maximum intensity of tropical cyclones in axisymmetric numerical model simulations. *Mon. Wea. Rev*., **137**, 1770–1789, https://doi.org/10.1175/2008MWR2709.1.

——, J. C. Wyngaard, and J. M. Fritsch, 2003: Resolution requirements for the simulation of deep moist convection. *Mon. Wea. Rev*., **131**, 2394–2416, https://doi.org/10.1175/1520-0493(2003)131<2394:RRFTSO>2.0.CO;2.

Coffer, B. E. and M. D. Parker, 2017: Simulated supercells in nontornadic and tornadic VORTEX2 environments. *Mon. Wea. Rev*., **145**, 149–180, https://doi.org/10.1175/MWR-D-16-0226.1.

Davies, J. M., 1998: On supercell motion in weaker wind environments. Preprints, *19th Conf. on Severe Local Storms*, Minneapolis, MN, Amer. Meteor. Soc., 685–688.

——, and R. H. Johns, 1993: Some wind and instability parameters associated with strong and violent tornadoes. Part I: Wind shear and helicity. *The Tornado: Its Structure, Dynamics, Prediction, and Hazards, Geophys. Monogr., No. 79*, Amer. Geophys. Union, 573–582, https://doi.org/10.1029/GM079p0573.

Doswell, C. A. III, 2007: Small sample size and data quality issues illustrated using tornado occurrence data. *Electronic J. Severe Storms Meteor.*, **2** (5), 1–16, https://doi.org/10.55599/ejssm.v2i5.10.

Eastin, M. D., and M. C. Link, 2009: Miniature supercells in an offshore outer rainband of Hurricane Ivan (2004). *Mon. Wea. Rev.*, **137**, 2081–2104, https://doi.org/10.1175/2009MWR2753.1.

Edwards, R., 1998: Storm Prediction Center support for landfalling tropical cyclones. Preprints, *23rd Conf. on Hurricanes and Tropical Meteor.*, Dallas, TX, Amer, Meteor. Soc, 53–56, https://www.spc.noaa.gov/publications/edwards/hurrspc.htm.

——, 2012: Tropical cyclone tornadoes: A review of knowledge in research and prediction. *Electronic J. Severe Storms Meteor.,* **7** (6), 1–61, https://doi.org/10.55599/ejssm.v7i6.42.

——, and R. L. Thompson, 1998: Nationwide comparisons of hail size with WSR-88D vertically integrated liquid water and derived thermodynamic sounding data. *Wea. Forecasting*, **13**, 277–285, https://doi.org/10.1175/1520-0434(1998)013<0277:NCOHSW>2.0.CO;2.

——, and A. E. Pietrycha, 2006: Archetypes for surface baroclinic boundaries influencing tropical cyclone tornado occurrence. Proc., 23rd Conf. on Severe Local Storms, St. Louis MO, Amer. Meteor. Soc., P8.2, https://www.spc.noaa.gov/publications/edwards/tcfronts.pdf.

——, and J.C. Picca, 2016: Tornadic debris signatures in tropical cyclones. Proc., *28th Conf. on Severe Local Storms*, Portland, OR, P162, https://www.spc.noaa.gov/publications/edwards/tctds.pdf.

——, and R. M. Mosier, 2022: Over a quarter century of TCTOR: Tropical cyclone tornadoes in the WSR-88D era. Proc., *30th Conf. on Severe Local Storms*, Santa Fe, NM, P171, https://www.spc.noaa.gov/publications/edwards/27yr-sls.pdf.

——, A. R. Dean, R. L. Thompson, and B. T. Smith, 2012a: Convective modes for significant severe thunderstorms in the contiguous United States. Part III: Tropical cyclone tornadoes. *Wea. Forecasting*, **27**, 1507–1519, https://doi.org/10.1175/WAF-D-11-00117.1.

——, ——, ——, and ——, 2012b: Nonsupercell tropical cyclone tornadoes: Documentation, classification and uncertainties. Proc., *26th Conf. on Severe Local Storms*, Nashville TN, 9.6, https://www.spc.noaa.gov/publications/edwards/nstc_sls.pdf.

——, J. G. LaDue, J. T. Ferree, K. Scharfenberg, C. Maier, and W. L. Coulbourne, 2013: Tornado intensity estimation: Past, present, and future. *Bull. Amer. Meteor. Soc*., **94**, 641–653, https://doi.org/10.1175/BAMS-D-11-00006.1.

——, G. W. Carbin, and S. F. Corfidi, 2015: Overview of the Storm Prediction Center. Proc., *13th History Symp.*, Phoenix, AZ, Amer. Meteor. Soc., 1.1, https://www.spc.noaa.gov/publications/edwards/spc-over.pdf.

——, M. S. Elliott, P. T. Marsh, and D. A. Speheger, 2022: Errors, oddities and artifacts in U.S. tornado data, 1995–2020. Proc., *30th Conf. on Severe Local Storms*, Amer. Meteor. Soc., Santa Fe, NM, 8.3B, https://www.spc.noaa.gov/publications/edwards/oddities.pdf.

Flournoy, M. D., and Couathors, 2024: Building a comprehensive database of observed supercells and tornadoes. Proc., *31st Conf. on Severe Local Storms*, Amer. Meteor. Soc., Virginia Beach, VA, P45, https://ams.confex.com/ams/31SLS/meetingapp.cgi/Paper/444693.

Hart, J. A., and W. D. Korotky, 1991: The SHARP workstation v1.30 users guide. NOAA/National Weather Service, 30 pp. [Available from NWS Eastern Region Headquarters, 630 Johnson Ave., Bohemia, NY 11716.]

Hersbach, H., and Coauthors, 2020: The ERA5 global reanalysis. *Quart. J. Roy. Meteor. Soc.*, **146**, 1999–2049, https://doi.org/10.1002/qj.3803.

Hill, E. L., W. Malkin and W. A. Schulz Jr., 1966: Tornadoes associated with cyclones of tropical origin—practical features. *J. Appl. Meteor.*, **5**, 745–763, https://doi.org/10.1175/1520-0450(1966)005<0745:TAWCOT>2.0.CO;2.

Hodges, K., A. Cobb, and P. L. Vidale, 2017: How well are tropical cyclones represented in reanalysis datasets? *J. Climate*, **30**, 5243–5264, https://doi.org/10.1175/JCLI-D-16-0557.1.

Kirkpatrick, C., E. W. McCaul Jr., and C. Cohen, 2007: The motion of simulated convective storms as a function of basic environmental parameters. *Mon. Wea. Rev*., **135**, 3033–3051, https://doi.org/10.1175/MWR3447.1.

Maddox, R. A., 1976: An evaluation of tornado proximity wind and stability data. *Mon. Wea. Rev*., **104**, 133–142, https://doi.org/10.1175/1520-0493(1976)104<0133:AEOTPW>2.0.CO;2.

Mahoney, E. A., and T. A. Niziol, 1997: BUFKIT: A software application toolkit for predicting lake effect snow. Preprints, *13th International Conf. on Interactive Information and Processing Systems (IIPS) for Meteorology, Oceanography, and Hydrology*, Long Beach, CA, Amer. Meteor. Soc., 388–391.

Markowski, P. M., 2016: An idealized numerical simulation investigation of the effects of surface drag on the development of near-surface vertical vorticity in supercell thunderstorms. *J. Amos. Sci*., **73**, 4339–4385, https://doi.org/10.1175/JAS-D-16-0150.1.

McCaul, E. W., Jr., 1991: Buoyancy and shear characteristics of hurricane-tornado environments. *Mon. Wea. Rev.*, **119**, 1954–1978, https://doi.org/10.1175/1520-0493(1991)119,1954:BASCOH.2.0.CO;2.

——, and M. L. Weisman, 2001: The sensitivity of simulated supercell structure and intensity to variations in the shapes of environmental buoyancy and shear profiles. *Mon. Wea. Rev*., **129**, 664–687, https://doi.org/10.1175/1520-0493(2001)129<0664:TSOSSS>2.0.CO;2.

Mosier, R. M., and R. Edwards, 2022: Visualization tools for the Storm Prediction Center's tropical cyclone tornado database. Proc., *30th Conf. on Severe Local Storms*, Amer. Meteor. Soc., Santa Fe, NM, P172, https://www.spc.noaa.gov/publications/mosier/tcttool.pdf.

Murakami, H., 2014: Tropical cyclones in reanalysis data sets. *Geophys. Res. Lett.*, **41**, 2133–2141, https://doi.org/10.1002/2014GL059519.

Nowotarski, C. J., J. Spotts, R. Edwards, S. Overpeck, and G. R. Woodall, 2021: Tornadoes in Hurricane Harvey. *Wea. Forecasting*, **36**, 1589–1609, https://doi.org/10.1175/WAF-D-20-0196.1.

Paredes, M., B. A. Schenkel, R. Edwards, and M. C. Coniglio, 2021: Tropical cyclone outer size impacts the number and location of tornadoes. *Geophys. Res. Lett.*, **48**, e2021GL095922, https://doi.org/10.1029/2021GL09592.

Rappaport, E. N., 2014. Fatalities in the United States from Atlantic tropical cyclones: New data and interpretation. *Bull. Amer. Meteor. Soc*., **95**, 341–346, https://doi.org/10.1175/BAMS-D-12-00074.1.

Ryzhkov, A. V., T. J. Schuur, D. W. Burgess, and D. S. Zrnić, 2005: Polarimetric tornado detection. *J. Appl. Meteor.*, **44**, 557–570, https://doi.org/10.1175/JAM2235.1.

Schenkel, B., and R. Hart, 2012: An examination of tropical cyclone position, intensity, and intensity life cycle within atmospheric reanalysis datasets. *J. Climate*, **25**, 3453–3475, https://doi.org/10.1175/2011JCLI4208.1.

——, N. Lin, D. Chavas, M. Oppenheimer, and A. Brammer, 2017: Evaluating outer tropical cyclone size in reanalysis datasets using QuikSCAT data. *J. Climate*, **30**, 8745–8762, https://doi.org/10.1175/JCLI-D-17-0122.1.

——, R. Edwards, and M. C. Coniglio, 2020: A climatological analysis of ambient deep-tropospheric vertical wind shear impacts upon tornadoes in tropical cyclones. *Wea. Forecasting*, **35**, 2033–2059, https://doi.org/10.1175/WAF-D-19-0220.1.

——, M. C. Coniglio, and R. Edwards, 2021: How does the relationship between ambient deep-tropospheric vertical wind shear and tropical cyclone tornadoes change between coastal and inland environments? *Wea. Forecasting*, **36**, 539–566, https://doi.org/10.1175/WAF-D-20-0127.1.

Schott, T. J., and Coauthors, cited 2024: Saffir–Simpson hurricane wind scale. NOAA/National Hurricane Center. [Available online at https://www.nhc.noaa.gov/aboutsshws.php.]

Schultz, L. A., and D. J. Cecil, 2009: Tropical cyclone tornadoes, 1950–2007. *Mon. Wea. Rev.*, **137**, 3471–3484, https://doi.org/10.1175/2009MWR2896.1.

Smith, B. T., R. L. Thompson, A. R. Dean, and P. T. Marsh, 2015: Diagnosing the conditional probability of tornado damage rating using environmental and radar attributes. *Wea. Forecasting*, **30**, 914–932, https://doi.org/10.1175/WAF-D-14-00122.1

Smith, T. M., and Coauthors, 2016: Multi-Radar Multi-Sensor (MRMS) severe weather and aviation products: Initial operating capabilities. *Bull. Amer. Meteor. Soc.*, **97**, 1617–1630, https://doi.org/10.1175/BAMS-D-14-00173.1.

Spratt, S. M., D. W. Sharp, P. Welsh, A. C. Sandrik, F. Alsheimer and C. Paxton, 1997: A WSR-88D assessment of tropical cyclone outer rainband tornadoes. *Wea. Forecasting*, **12**, 479–501, https://doi.org/10.1175/1520-0434(1997)012<0479:awaotc>2.0.co;2.

Taszarek, M., H. E. Brooks, and B. Czernecki, 2017: Sounding-derived parameters associated with convective hazards in Europe. *Mon. Wea. Rev*. **145**, 1511–1528, https://doi.org/10.1175/MWR-D-16-0384.1.

——, B. Czernecki, and P. Szuster, 2023: thundeR—a rawinsonde package for processing convective parameters and visualizing atmospheric profiles. Proc*., 11th European Conf. on Severe Storms*, Bucharest, Romania, European Severe Storms Laboratory, https://doi.org/10.5194/ecss2023-28.

Thompson, R. L., R. Edwards, J. A. Hart, K. L. Elmore, and P. Markowski, 2003: Close proximity soundings within supercell environments obtained from the Rapid Update Cycle. *Wea. Forecasting*, **18**, 1243–1261, https://doi.org/10.1175/1520-0434(2003)018<1243:CPSWSE>2.0.CO;2.

Trapp, R. J., G. J. Stumpf, and K. L. Manross, 2005: A reassessment of the percentage of tornadic mesocyclones. *Wea. Forecasting*, **20**, 680–687, https://doi.org/10.1175/WAF864.1.

Trier, S. B., D. A. Ahijevych, D. Carroll-Smith, G. H. Bryan, and R. Edwards, 2023: Composite mesoscale environmental conditions influencing tornado frequencies in landfalling tropical cyclones. *Wea. Forecasting*, **38**, 2481–2508, https://doi.org/10.1175/WAF-D-22-0227.1.

Verbout, S. M., D. M. Schultz, L. M. Leslie, H. E. Brooks, D. J. Karoly and K. L. Elmore, 2007: Tornado outbreaks associated with landfalling hurricanes in the North Atlantic Basin: 1954-2004. *Meteor. Atmos. Phys*., **97,** 1–4, https://doi.org/10.1007/s00703-006-0256-x.

Weiss, S. J., 1987: Some climatological aspects of forecasting tornadoes associated with tropical cyclones. Preprints, *17th Conf. on Hurricanes and Tropical Meteor.*, Miami, FL, Amer. Meteor. Soc., 160–163.